A Wavelet Transform-Based Approach for Joint Tracking in Gas Metal Arc Welding

A new system was developed for joint tracking and control of the GMA welding process based on CCD sensors without an external light source

BY J. X. XUE, L. L. ZHANG, Y. H. PENG, AND L. JIA

ABSTRACT. Effective tracking of the weld joint is crucial to the development of a high-performance control system for the gas metal arc welding (GMAW) process. This paper presents a new approach to effectively track weld joints based on charge coupled device (CCD) sensors. Due to the presence of spatter, dust, and strong arc noises in welding environments, it has proved to be difficult to detect the weld joint from the CCD images captured in real time. In order to improve the robustness of weld joint tracking, this paper presents a novel approach, based on the Bubble and M-band wavelet transform, for detecting the image edge of molten weld pools from the images captured during GMAW. The experimental results show that the effectiveness of the proposed method in detecting the edges of molten weld pools and identifying weld joints even when the welding images are presented with much noise. Based on the weld joint identification, a PID control approach is employed to manipulate the welding gun in order to produce a desired weld joint. The control experiments demonstrate that, based on the proposed joint tracking, the control of an S-shaped weld joint has been effectively delivered with good precision.

Introduction

Extensive research has been performed for developing efficient and effective techniques for tracking and controlling the welding process. Many systems have been developed in research laboratories; however, they are still challenged by a variety of uncertainties and complexities when used in industrial environments. The objective of this research is to develop effective and efficient algorithms for the online identification of weld joints, based on the processing of the molten pool images and to facilitate the intelligent control of the welding process (Refs. 1–4). For the development of systems with great value for industrial applications, it is desired to develop approaches capable of tracking the weld joint without using an additional light source (i.e., directly using the light produced by the welding arc) in order to reduce the cost, although it would increase the complexity and difficulty of weld joint tracking.

Most of the existing techniques have been developed for tracking and control of the gas tungsten arc (GTA) and gas metal arc (GMA) welding processes. The arc sensing method is an effective technique that can identify weld defects and track weld joints exactly through arc scanning. Based on this, many joint tracking systems have been developed and practically applied for gas metal arc and CO_2 welding. In practice, the arc sensor requires a set of weaving arc devices, which has a complex structure and is more easily implemented with a welding robot. It is restricted on the aspect of mechanism and its weaving frequency is rather low, so it is only suitable for bevels, corner joints, lap joints, etc., and is not effective for high-speed and sheet joint tracking of butt joints. Vision sensor methods can directly observe the area of the weld joint to facilitate artificial intelligence (Refs. 5–7). In the GMAW process, the molten pool images are presented with much noise (such as bright spots and lines due to spatters). As a result, the weld joint is usually very difficult to identify in real time. Kim et al. (Ref. 8) developed a robot visual tracking system for arc welding in which a CCD sensor is used to capture the positional information of the joint. In this system, an additional laser light was used. Gao et al. (Ref. 9) developed a fuzzy logic controller for a welding robot. Tao and Levick (Ref. 10) developed a method to assess the feedback variables for arc joint tracking in a robotic GMAW system. They investigated the use of a welding power source for feedback control of welding current and voltage. Cheng et al. (Ref. 11) developed an image processing algorithm for joint detecting and tracking in a pulse GTAW process. Their algorithm has been tested when the current waveform was controlled under a strictly level (the molten pool image was presented with very little arc noise). Recently, Kim et al. (Ref. 12) and Matsui et al. (Ref. 13) developed a three-dimensional sensor system for the recognition of operating conditions and weld joint tracking. Matsui's GMAW system has been tested on thin steel sheets.

For effective identification of the weld joint, this paper proposes a new approach to detect the edge of molten pools from the images obtained during the GMAW process by applying wavelet transform techniques to extract the space and frequency information of the images. Based on the excellent capability of extracting the space-frequency information from images (Refs. 14, 15), the arc welding image signals with strong noise can be depicted with the wavelet coefficients through the process of multiresolution decomposition. On the other hand, the image noise can be eliminated according to the signal energy estimated based on the associated wavelet coefficients.

In this study, a Windows®-based system has been developed for joint tracking control of the GMAW process, in which a high-performance A/D image converter and a novel edge detection algorithm are embedded. The wavelet transform algorithm is

*JIA XIANG XUE (*mejiaxue@scut.edu.cn*) is with School of Mechanical Engineering, South China University of Technology, Guangzhou, China. LI LING ZHANG is with Department of Mechanical and Power engineering, Nanchang Institute of Technology, Nanchang, China. YONG HONG PENG is with University of Bradford, UK. LIN JIA is with, South China University of Technology Library, Guangzhou, China.*

KEYWORDS

Gas Metal Arc Welding
Joint Tracking
Process Control
Process Monitoring
C-Mn Steels

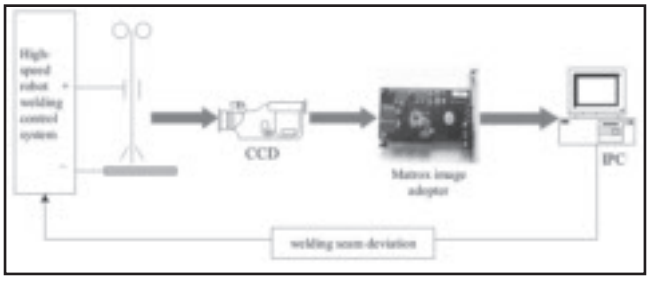

Fig. 1 — The developed intelligent weld tracking and control system.

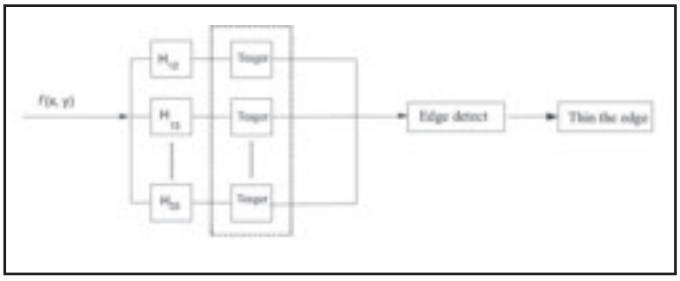

Fig. 3 — The image edge detecting flow with M-band wavelet transform.

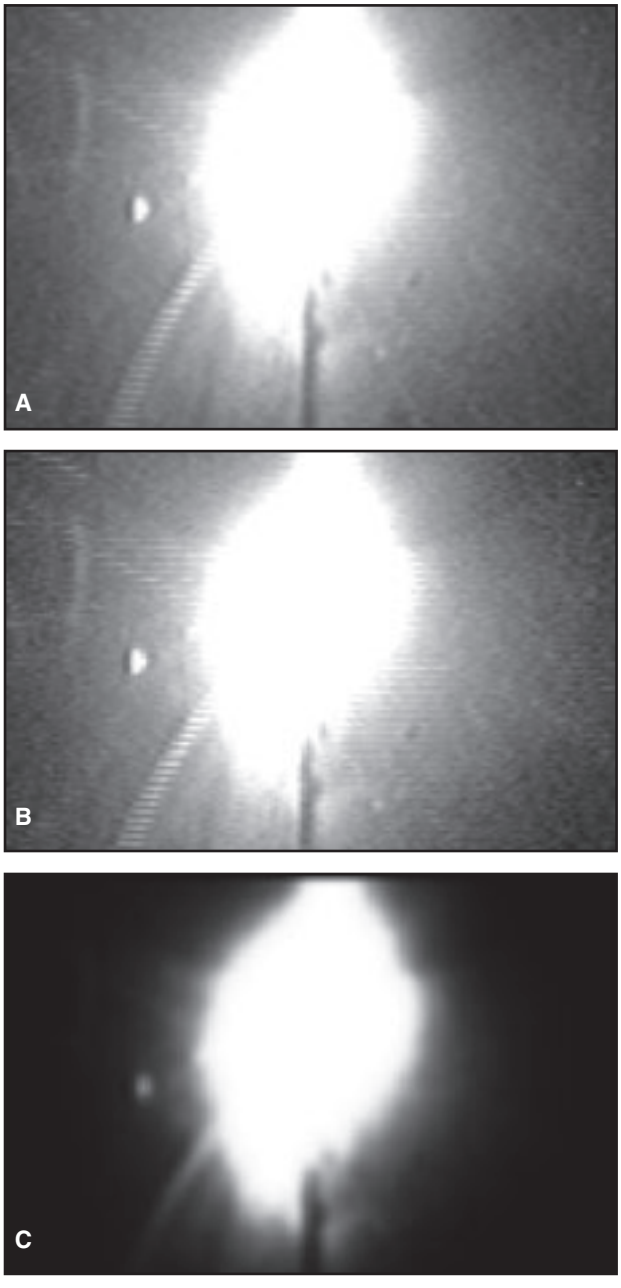

Fig. 2 — Result of image preprocessing: filtering and squaring. A — The original welding image; B — the result after median filtering; C — the result after filtering and squaring.

modified so as to fulfill the requirements of precision, speed, and noise elimination needed for real-time tracking and control of a GMAW joint. The system can automatically track and control the weld joint after the starting point of the welding process is given.

As shown in Fig. 1, this system consists of five steps:

1. A CCD sensor system is used to capture the original images of the weld joint and the foreside of the molten pools;
2. A high-resolution A/D converter is employed to digitalize the original image;
3. The digital images are then processed to detect the edge of the molten pools, for which a novel algorithm based on wavelet transform is proposed in this paper;
4. The central track of the weld joint is estimated based on the edges of the molten pools;
5. Finally, a PID controller is applied to deliver the control signal to the three-dimensional servo system to manipulate the welding gun to produce a weld joint close to the desired track as accurately as possible.

Edge Detection with M-Band Wavelet Transform

M-Band Wavelet Transform

The region of the image captured by CCD is 640 × 480 pixels. To ensure the controlling effectiveness, only the central image of the molten pool, which was sized 90 × 120 pixels, was processed. Conventional approaches to applying wavelet transform techniques for the detection of image edges are to use dyadic wavelet transform to decompose the image and then to detect the object edge with Mallat Scheme of Local Modulus Maxima. These conventional approaches have been applied successfully for general image processing (Refs. 16–21). However, the conventional dyadic wavelets transform is not suitable for processing narrowband and high-frequency signals (Ref. 22). The orthogonal dyadic wavelets can only have either compactly supported property or linear-phase (except Harr wavelet, as concerning real filter) (Ref. 23), which are

Table 1 — Four-Band Wavelet Taper Decomposed Structure

LL	H_1L	H_2L	H_3L
LH_1	H_{11}	H_{21}	H_{31}
LH_2	H_{12}	H_{22}	H_{32}
LH_3	H_{13}	H_{23}	H_{33}

Table 2 — Filter Coefficients

h_n	$g^1{}_n$	$g^2{}_n$	$g^3{}_n$
0.114701	0.026913	0.135299	–0.076641
0.385299	–0.326641	–0.218254	0.076641
0.576641	–0.488852	–0.326641	0.114701
0.576641	0.135299	0.680194	–0.385299
0.385299	0.680194	–0.135299	0.576641
0.114701	0.326641	–0.488852	–0.576641
–0.076641	–0.218254	0.326641	0.385299
–0.076641	–0.135299	0.026913	–0.114701

Table 3 — Experimental Parameters of Tracking Control

Maximum horizontal tracking error	0.29 mm
Maximum vertical tracking error	0.58 mm
Maximum tracking error	0.40 mm
Average tracking error	0.27 mm

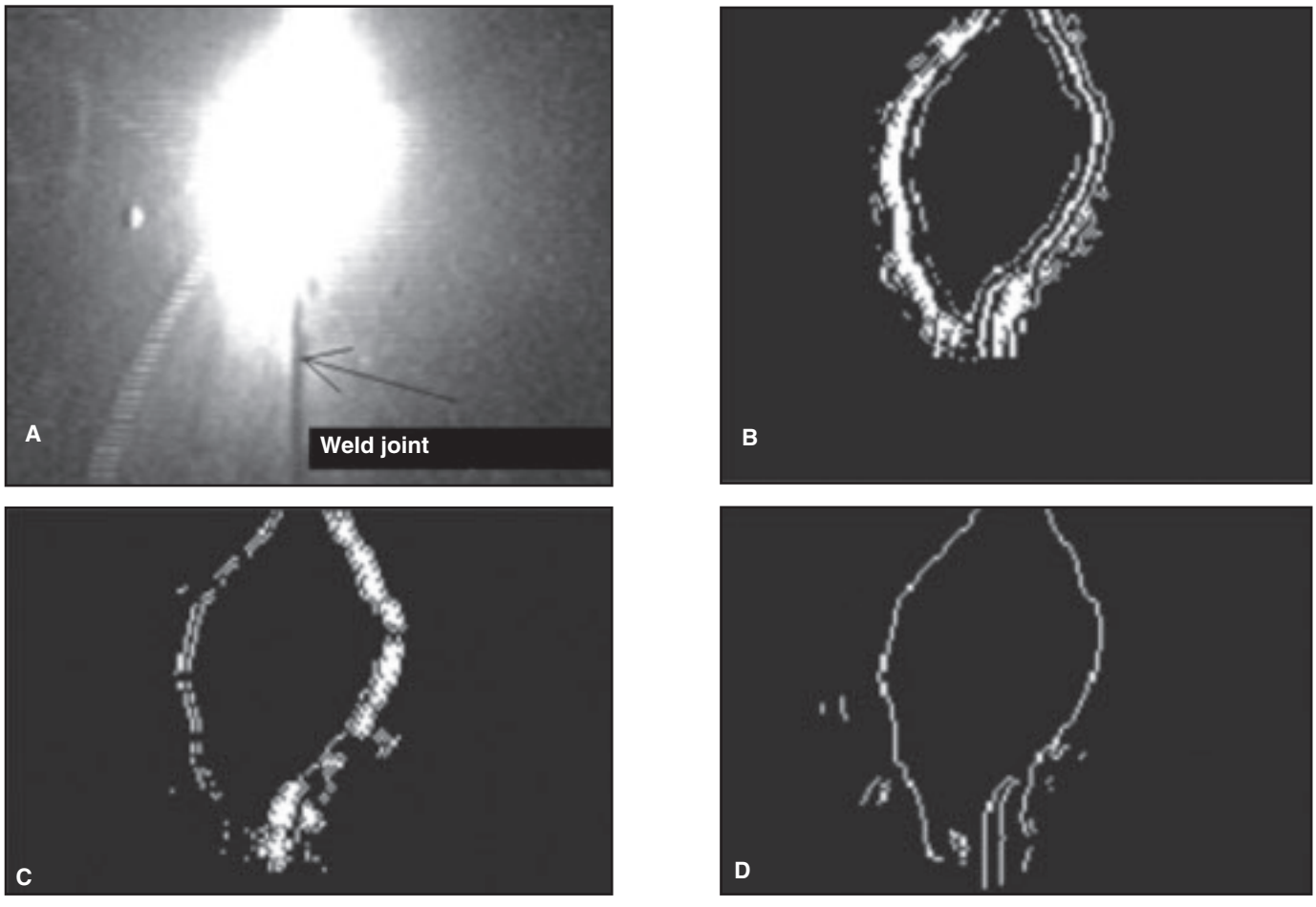

Fig. 4 — The results of molten pool image edge detection with M-band wavelet transform. A — Molten weld pool; B — horizontal result; C — vertical result; D — synthetic result.

both useful properties for image processing so as to ensure not distorting the quality of images. M-band wavelet transform, compared to dyadic orthogonal wavelet transform, has three useful merits, which can be used effectively in image edge detection (Ref. 22): 1) it has a narrower frequency band at the high-frequency band; 2) its energy is more concentrated; 3) an orthogonal M-band wavelet can be a compactly supported and linear-phase one.

The construction of the M-band discrete wavelet is similar to that of the dyadic wavelet (Refs. 24, 25), which is derived from a two-scale equation as:

$$\phi(x)=\sum_{n\in Z} h_n \phi(Mx-n) \qquad (1)$$

where M is an integer $M \geq 2$, and $\phi(x)$ is called as a scale function, h_n are the scale coefficients. If $\phi(x)$ is known, (M-1) wavelet could be generated by

$$\psi^i(x)=\sum_n g_n^i \phi(Mx-n), \quad i=1,2,\ldots,(M-1) \qquad (2)$$

where $\{g^i_n\}$ are $(M–1)$ groups of wavelet decomposition coefficients. Usually, the relation between $\{g^i_n\}$ and $\{h_n\}$ is unknown. Let us define the scale functions as

$$\phi_{m,n}(x)=M^{-m/2}\phi(M^{-m}x-n),$$
$$\psi^i_{m,n}(x)=M^{-m/2}\psi^i(M^{-m}x-n). \qquad (3)$$

For a discrete signal $f(x)$, its wavelet transforms are

$$Sf_{m,n}=\langle f(x),\phi_{m,n}(x)\rangle,$$
$$Df_{i,m,n}=\langle f(x),\psi^i_{m,n}(x)\rangle, \qquad (4)$$

then the $Sf_{m-1,n}$ and $Df_{i,m-1,n}$ can be calculated by the recursions as follows:

$$Sf_{m-1,n}=M^{-1/2}\sum_n h_n Sf_{m,n}$$
$$Df_{i,m-1,n}=M^{-1/2}\sum_n g_n^i Sf_{m,n}$$
$$i=1,2,\ldots,M-1 \qquad (5)$$

Therefore, for a signal $f(x)$, we can obtain the associated multiscale decomposition and reproduction of M-band wavelet transform. For processing two-dimensional images, M-band wavelet transform is performed based on M^2 filter-pairs. The M^2-channel separable wavelet transform can be obtained by the tensor product of M-band one-dimension wavelet filters, which are denoted by $\phi_{m,n}$. The results obtained by these M^2 filter pairs contain useful edge characteristics defined at different scales. In this paper, M=4 is used, namely an image is decomposed into 16 sub-bands accordingly. As shown in Table 1, each sub-band is

$$LL=\varphi_{m,n}\varphi_{m,n}, LH_j=\phi_{m,n}\psi^j_{m,n}$$
$$H_iL=\psi^i_{m,n}\varphi_{m,n}, H_{i,j}=\psi^i_{m,n}\psi^j_{m,n},$$
$$i,j=1,2,3 \qquad (6)$$

The M^2 filter-pairs used in this paper are from 8-tap 4-band discrete wavelet transform (Ref. 26). Table 2 shows the associated coefficients.

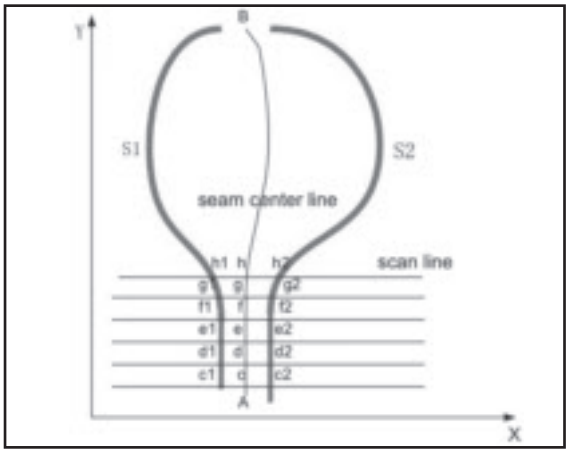

Fig. 5 — The method for detecting welding joint center.

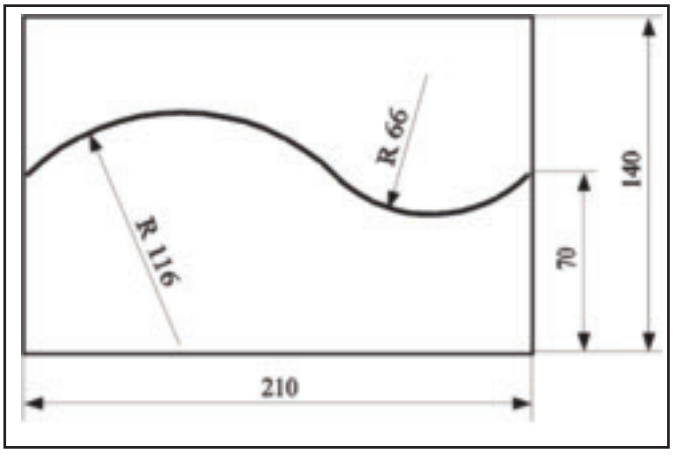

Fig. 6 — The geometry chart of the weld joint.

The Proposed Edge Detection Algorithm

The image decomposition needs to be modified in order to fulfill the computation requirement in real-time applications. In this study, an image is processed in the horizontal and the vertical directions separately. This simplification facilitates the use of a one-dimensional filter to process the image serially, and enables the edge detection to be performed online.

In principle, the frequency response perpendicular to the edge direction is the strongest, whereas the more parallel to the edge direction, the smaller is the frequency response (Refs. 27, 28). This inspired us to use a high-pass filter along the edge direction, and to use the low-pass filter upright the edge direction. Furthermore, as only the results of the high-pass filter make sense for edges detection, the results produced by the low-pass filter can then be ignored.

In order to achieve robust edge detection, the noise and pseudo-edges are eliminated in a preprocessing step. In this study, the Median filter (Ref. 29), which is a well-known nonlinear approach in image processing, to eliminate noise while protecting the edges from being blurred. Particularly, the median smoothing mask in a 3 × 3 neighborhood is used in this study:

$$\frac{1}{10}\begin{bmatrix}1&1&1\\1&2&1\\1&1&1\end{bmatrix}. \qquad (7)$$

After applying the median filter, it is seen there is still halation around the molten pools, which affects the effectiveness of the edge detection, as illustrated in Fig. 2B. To eliminate the halation, we square the grey value for each pixel:

$$f'(x,y)=\left[f(x,y)\times f(x,y)\right]/255, \qquad (8)$$

where $f(x,y)$ denotes the gray level of the image pixel located at (x, y). Figure 2C shows the preprocessing result of one image, which shows the noise and halation have been effectively eliminated and the molten pool is clearly reveled.

After preprocessing the image, the edge of a molten pool is detected based on the Teager's energy operator (Refs. 30, 31) defined on the decomposition of an image. The one-dimensional form of the Teager's energy is

$$T\left[f(t)\right]=\left(\frac{df(t)}{dt}\right)^2-f(t)\frac{d^2f(t)}{dt^2} \qquad (9)$$

while in discrete domain, it becomes

$$T\left[f(n)\right]=f^2(n)-f(n+1)f(n-1). \qquad (10)$$

As stated previously, an image is processed by one-dimensional wavelet transform, respectively, in each direction. After decomposing an image $f(x,y)$, a total of $M \times M$ different sub-band components are produced. By applying the Teager operator to calculate the energies of these sub-band components, the associated edge can then be detected in terms of the energy of the sub-band components. The components having high energy are considered as edge whereas the components having low energy are considered as the pseudo-edge or noise. The image edge detecting flow chart with M-band wavelet transform is shown in Fig. 3, which particularly consists of the following steps:

1. Given an image $f(x,y)$, the median filter (Equation 7) and the square operator (Equation 8) are used to preprocess the image;

2. The wavelet operators LH_j, H_{ij}($i \neq j$, $i, j=1,2,\ldots M-1$), as shown in Equation 6 are used to decompose it in the horizontal direction;

3. Apply the Teager operator to calculate the energy of each sub-band, and select an appropriate threshold to eliminate the noise components;

4. Extract the maximum wavelet transform coefficients and add them up to achieve the high-pass filtering and form wavelet transform maximum in the horizontal direction, from which the image edge information in horizontal direction is thus extracted;

5. The similar steps of numbers 2–4 are used to process the image $f(x,y)$ to extract the edge information in the vertical direction, but the wavelet operators are changed as H_iL, H_{ij} ($i \neq j$, $i, j=1,2,\ldots M-1$);

6. The transformed results in both the horizontal and vertical directions are then combined;

7. The outputs of step 6 are then compared with a predefined threshold t_0. The points with values bigger than t_0 are considered as edge points, and are connected to generate the image edge;

8. If the edges generated by step 7 are a little thick, it is necessary to thin them in order to estimate the position of the weld joint more accurately. To do so, we set a smaller detecting range $[t_1, t_2]$ of pixel values. All the edge pixels generated by step 7 are scanned again with this range. By marking and connecting these pixels whose values are in the range, a final and effective edge of the molten pool is then produced.

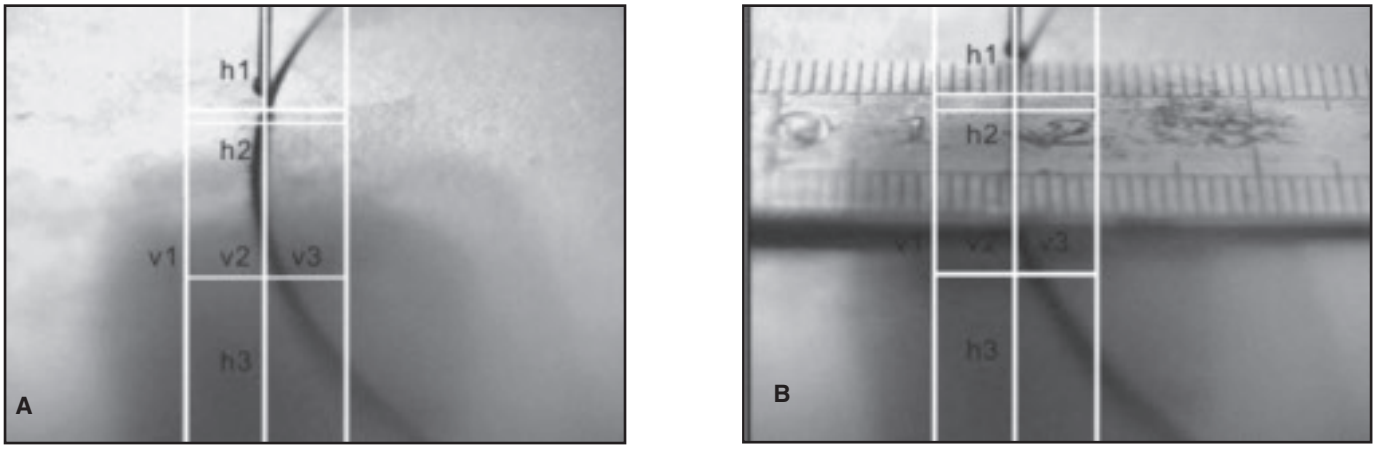

Fig. 7 — Pictures of the following: A — Original position of the weld joint; B — the calibration.

Fig. 8 — The front photo of the practical joint tracking.

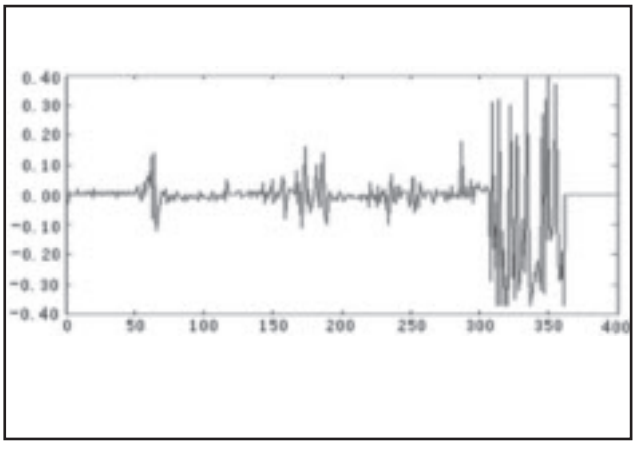

Fig. 9 — The curve of tracking deviation.

Joint Tracking and Control of GMAW

Joint Tracking Based on Molten Pool Edge Detection

The procedure of the proposed edge detection algorithm for weld joint tracking is illustrated by the example shown in Fig. 4. Figure 4A shows the original image of a welding molten pool and the weld joint. Figure 4B and C show, respectively, the results of the edge of the molten pool detected in horizontal and vertical directions. Both of them are produced by combining the results of three sub-band components with the highest Teager energies. It is shown that the joint edge detected in the horizontal direction is clearer than the edge detected in the vertical direction (which is not so obvious in many ranges).

As the orthogonal M-band wavelet transform has a linear phase, the results of the edge detected in different directions can be added up directly, without any positional deviation. Figure 4D is the synthetic result based on combining the results obtained in horizontal and vertical directions. Comparing Fig. 4D with the results of Fig. 4B and C, the result of edge detection is significantly improved. These results demonstrate that the edge information obtained in the vertical and horizontal directions can well complement each other, and the proposed method is able to improve obviously the detection of edges of molten pools.

Based on the detected edge of molten pools, the weld joint track, defined by a set of central points of molten pools, can then be determined. To do so, the CCD scans successively along the X-axis with a distance of three pixels. As illustrated by Fig. 5, based on the detected edges of a molten pool (denoted by curves S1 and S2), each scan line generates a pair of characteristic points such as c1, c2, and d1, d2, and so on, and the associated central points, such as points *c* and *d* defined by c1, c2, and d1, d2. The weld joint track is then obtained by connecting all these central points, such as the curve AB shown in Fig. 5.

Control of Weld Joint

In our system, the control variable is the positional deviation of the welding torch, which is measured at the upright to the weld joint's direction. When the weld joint has been identified by means of the edge detection algorithm, the position of welding torch is adjusted by a PID close control loop. The controller adjusts the torch movement in real time according to the positional deviation, in order to produce a weld joint as close as possible to the desired weld joint. The PID controller used a discrete form as

$$u(t) = k_p e_k + \frac{Tk_p}{T_i}\sum_{j=1}^{k} e_j + \frac{k_p T_d}{T}\left(e_k - e_{k-1}\right) \qquad (11)$$

where $K_p = 0.6$, $T_i = 0.25$, $T_d = 0.05$, $T = 0.1$.

Experimental Results

Experimental Condition

A 2-mm-thick Q235 steel workpiece with a narrow joint was used in our experiments to make the tracking method more

fit for industrial practice. The weld joint is shown in Fig. 6. The setup of the welding experiment conditions was as follows:

Shield gas: 80%Ar+20%CO_2
Gas flow: 15 L/s
Welding speed: 5 mm/s
Arc voltage: 18.5–19 V
Welding current: 90–110 A
Welding gun type: vertical gun
Wire type: CHW-50C6
Wire diameter: ϕ0.8 mm
Power source: NB200B-IGBT inverter
Load duty: 60%.

The CCD sensor-based image-collection system is configured by a Pentium® IV CPU, a 256M memory, a Matrox image adopter, and a PIH-7912 camera with collecting image rate 30 frames/second. From the hardware point of view, we used a color filter to eliminate arcs of a specific wavelength. The main parameters of PIH-7912 are as follows:

Effective Pixels: 795 (H) × 596 (V) [NTSC];
Resolution: 600 TV lines
Shutter: 1/60 to 1/10000 s (auto).

The CCD visual sensor is rigidly fixed on the welding gun and adjusted as parallel as possible to the welding gun so that the gun would not cover the weld joint during operation. This setup helps to reduce the influence of the welding gun, and enlarge the welding image's visual field. However, because of a fixed gun with the certain angle, there inevitably exists distortion in the collected image including the shape of the weld joint and molten pools. The distortion caused extra deviation in welding control, but the associated deviation was a systemic static error and thus can be determined through off-line experiments.

Image Calibration

In joint tracking and control, it is necessary to determine the starting point of the joint curve and initialize the welding gun position. The method used in this study is illustrated in Fig. 7. First, the welding wire was moved to a predetermined starting point of the joint (as denoted in Fig. 7A). The horizontal angle of the CCD was adjusted so that it superposes the welding wire with the vertical datum line (v2) as shown in Fig. 7. Two vertical lines (v1, v3) were then marked beside v2 with a distance of 50 image pixels. The CCD was then adjusted to focus on the areas between v1 and v3. Second, two horizontal lines (h1, h2) were marked with a distance of ten image pixels beside the starting points. The CCD was adjusted in the vertical direction so that the terminal of the welding wire was seen between the lines of h1 and h2. Referring to another horizontal line (h3) under h2 with a distance of 100 image pixels, the CCD was adjusted to focus on the area between the lines h1 and h3. As a result, the section of v2 between h1 and h2 is almost coincident with the weld joint. In this way, the original position of the weld joint can be estimated accurately.

The physical distance associated with every pixel point was calibrated in the way shown in Fig. 7B. Using a ruler to measure the distance between v1 and v3 (as shown in Fig. 7B, the distance is 10 mm). Dividing this distance by the number of pixels between v1 and v3 (100 pixels for the case shown in Fig. 7B), then we can get the calibrating distance of every pixel point. For the case shown in Fig. 7, the calibrating distance is 0.1 mm per pixel.

Experimental Results of Tracking and Control

In our experiment, the range of identified weld joint widths was 0.1–0.5 mm. By changing the CCD focus or adopting the sub-pixel identifying technique, the identification precision can be further improved. In practice, the weld joints are usually wider than 0.1 mm, which means our method can satisfy practical requests. Figure 8 shows tracking and control results for the desired weld joint shown in Fig. 6, and tracking accuracy follows in Table 3.

Figure 9 shows the curve of tracking deviation produced by the PID control system. The deviation is calculated indirectly according to the revolution of the step motor. The Y-axis denotes the revolution of the motor, each revolution corresponding to 1 mm in the Y-axis. The X-axis denotes the times of sample (the sampling period is 100 ms particularly). Figure 9 indicates that the deviations vary from region to region. In detail, the deviations in the second half curve are bigger than those in the first half curve, especially during the last 50 sampling periods. The main reason of aforementioned situation is the breadth change of joint caused by thermal deformation in the welding process. Furthermore, deviation is also obvious between two joint arcs (from 16 to 18 s). The reason is that the big curvature increases the adjusting force of the mechanism.

Conclusions

This paper presents a new system for joint tracking and control of the GMA welding process based on CCD sensors without an external light source. An integrated software and hardware system has been developed for image collection and processing, and weld joint tracking based on wavelet transform. Based on the experimental results, we summarize the following important conclusions:

1. A novel method based on the median filter and square operation was developed for the preprocessing of molten pool images of GMAW in order to eliminate the noise caused by the strong arc and the spatters.

2. An effective M-band wavelet transform-based approach was developed for the edge detection of the molten pools and the weld joint.

3. The experiments on S-shaped weld joints demonstrated the effectiveness of the tracking and control system. The system is capable of detecting and tracking the weld joint automatically in real time.

4. One further development for this system is the enhancement of the system performance, for example, to reduce the error of weld joints and the improvement of system reliability. In addition, we will attempt to use a fuzzy control system to replace the PID controller in order to develop an intelligent system able to address various uncertainties presented in the industrial environments.

Acknowledgments

The authors wish to acknowledge Prof. Shisheng Huang for providing the experiment equipment. The authors are also grateful to Haibao Li, Ruolei Zhu, and Pengjun Mao for their helpful support during this work.

This research is supported by Guangdong Natural Science Fund in China (under Grant 000380 and 04020100).

References

1. Kovacevic, R., Zhang, Y. M., and Li, L. 1995. Monitoring of weld joint penetration based on weld pool geometrical appearance. *Welding Journal* 74(10): 317–329.

2. Kuo, H.-C., and Wu, L.-J. 2002. An image tracking system for welded seams using fuzzy logic. *Journal of Materials Processing Technology* 120: 169–185.

3. Suga, Y., Sato, Y., Naruse, M., Kojima, K., and Ogawa, K. Recognition of the weld line by a visual sensing system and weld line tracking in automatic welding of thin aluminum plates. *Welding International* 7(4): 273–279.

4. Yu, J. Y., and Na, S. J. A study on vision sensors for seam tracking of height-varying weldment. Part 1: Mathematical model. *Mechatronics* 7(7): 599–612.

5. Kim, J. W., and Na, S. J. 1991. A study on an arc sensor for gas metal arc welding of horizontal fillets. *Welding Journal* 69(8): 216–221.

6. Nomura, H., Sugitani, Y., and Tamaoki, N. 1987. Automatic real-time bread height control with arc sensor. *Transactions of Japan Welding Society* (2): 43–50.

7. Kim, J. W., and Na, S. J. 1993. A self-organizing fuzzy control approach to arc sensor for weld joint tracking in gas metal arc welding of butt joints. *Welding Journal* 72(20): 60–66.

8. Kim, J. S., Son, Y. T., Cho, H. S., and Koh, K. I. 1995. A robust method for vision-based seam tracking in robotic arc welding. *Proceedings of the 1995 IEEE International Symposium*

363–368.

9. Xiangdong, G., Yamamoto, M., and Mohri, A. 1997. Application of fuzzy logic controller in the seam tracking of arc-welding robot. *23rd International Conference* 3: 1367–1372.

10. Tao, J., and Levick, P. 1999. Assessment of feedback variables for through the arc seam tracking in robotic gas metal arc welding. *Proceedings of the 1999 IEEE International Conference* 4: 3050–3052.

11. Nian, C., Zhen-guo, S., and Qiang, C. 2001. A visual sensor based weld seam tracking method for precision pulse TIG weld. *Transactions of the China Welding Institution* 22(4): 17-s to 20-s.

12. Kim, M. Y., Cho, H. S., and Ki, J-h. 2001. Neural network-based recognition of navigation environment for intelligent shipyard welding robots. *Proceedings of 2001 IEEE/RSJ International Conference* 1: 446–45.

13. Matsui, S., and Goktug, G. 2002. Slit laser sensor guided real-time seam tracking arc welding robot system for non-uniform joint gaps. *2002 IEEE International Conference* 1: 159–162.

14. Cotronei, M., Montefusco, L. B., and Puccio, L. 1998. Multiwavelet analysis and signal processing. *IEEE Trans. On Circuits and Systems — II: Analog and Digital Processing* 45(8): 970-s to 987-s.

15. Witkin, A. 1983. Scale space filtering. *Proc. Int. Joint Conf. Artificial Intell.*

16. Meyer, Y. 1992. *Wavelets and Operators.* Cambridge University Press.

17. Fusheng, Y. 1999. *Engineering Analysis and Application of Wavelet Transform.* Beijing, Academic Press (in Chinese).

18. Berman, Z., and John, S. 1993. Properties of the multiscale maxima and zero-crossings representations. *IEEE Trans on Signal Processing* 41(12): 3216-s to 3231-s.

19. Mallat, S., and Hwang, W. L. Singularity detection and processing with wavelets. *IEEE Trans. Inform. Theory* 38(2): 617-s to 643-s.

20. Canny, J. 1986. A computational approach to edge detection. *IEEE Trans. On Pattern Analysis and Machine Intelligence* 8(6): 619-s to 691-s.

21. Shensa, M. J. 1992. The discrete wavelet transform: Wedding the A Trous and Mallat algorithm. *IEEE Trans. on Signal Processing* 40(10): 2464-s to 2482-s.

22. Zhang, J. K., and Bao, Z. 1999. The theory of M-band orthogonal compactly supported wavelet. *China Science (E)* 29(5): 427-s to 441-s.

23. Xia, X. G., and Zhang, Z. 1993. On sampling theorem, wavelets, and wavelet transforms. *IEEE Trans on Signal Processing* 41(12): 3524-s to 3535-s.

24. Steffen, P., Heller, P. N., Gopinath, R. A., and Burrus, C. S. 1993. Theory of regular M-band wavelet bases. *IEEE Transactions on Signal Processing* 41(12): 3497-s to 3511-s.

25. Zou, Z., and Tewfik, A. H. 1992. Discrete orthogonal M-band wavelet decomposition. *Proc. ICASSP,* San Francisco, Calif. 4(4): 605–608.

26. Aydin, T., Yemez, Y., Anarim, E., and Sankur, B. 1996. Multidirectional and multiscale edge detection via M-band wavelet transform. *IEEE Transactions on Image Processing* 5(9): 1370-s to 1377-s.

27. Ikonomopoulos, A., and Kunt, M. Image coding via directional filtering. *IEEE Trans. On Signal Processing* 8(2): 179–202.

28. Tang, X. H., Gong, Y., and Gong, Y. H. 1997. Image edge detection by using M-band wavelet transform. *Journal of UEST of China* 26(2): 117-s to 120-s.

29. Wang, Y., and Mitra, S. K. 1991. Edge detection based on orientation disturbance of gradient images. *1991 IEEE International Conference on Acoustics, Speech, and Signal Processing* 4: 2569–2572.

30. Akarun, L., and Haddad, R. A. 1993. Adaptive decimated median filters for image processing. *1993 IEEE International Conference on Acoustics, Speech, and Signal Processing* 5: 69–72.

31. Alkin, O., and Caglar, H. 1995. Design of efficient M-band coders with linear-phase and perfect-reconstruction properties. *IEEE Transactions on Signal Processing* 43(7): 1579-s to 1590-s.

Correction to Article Titled 'Fabrication of a Carbon Steel-to-Stainless Steel Transition Joint Using Direct Laser Deposition — A Feasibility Study,'

by J. D. Farren, J. N. DuPont, and F. F. Noecker

This article was published in the March 2007 edition of the Welding Journal and utilized the WRC Constitution Diagram as an aid to interpreting microstructures that formed between a transition joint. The transition joint had carbon steel on one end and stainless steel on the other end. The diagram appears in Figure 9A, and experimental composition measurements were plotted directly on the diagram. In this diagram, the lines of constant ferrite contents were mistakenly labeled as percent ferrite. The WRC Diagram uses Ferrite Number, not percent ferrite. Thus, the percent values labeled on the diagram are incorrect, and the values actually represent Ferrite Number.

Dear Readers:

The *Welding Journal* encourages an exchange of ideas through letters to the editor. Please send your letters to the Welding Journal Dept., 550 NW LeJeune Rd., Miami, FL 33126. You can also reach us by FAX at (305) 443-7404 or by sending an e-mail to Kristin Campbell at *kcampbell@aws.org*.